Solar Phys (2017) 292:134
DOI 10.1007/s11207-017-1163-7

RADIO AND SPACE-BASED OBSERVATIONS

Predicting Flares and Solar Energetic Particle Events: The FORSPEF Tool

A. Anastasiadis[1] · A. Papaioannou[1] · I. Sandberg[1] · M. Georgoulis[2] · K. Tziotziou[1] · A. Kouloumvakos[3] · P. Jiggens[4]

Received: 15 May 2017 / Accepted: 29 August 2017

Abstract A novel integrated prediction system for solar flares (SFs) and solar energetic particle (SEP) events is presented here. The tool called forecasting solar particle events and flares (FORSPEF) provides forecasts of solar eruptive events, such as SFs with a projection to occurrence and velocity of coronal mass ejections (CMEs), and the likelihood of occurrence of an SEP event. In addition, the tool provides nowcasting of SEP events based on actual SF and CME near real-time data, as well as the SEP characteristics (*e.g.* peak flux, fluence, rise time, and duration) *per* parent solar event. The prediction of SFs relies on the effective connected magnetic field strength ($B_{\rm eff}$) metric, which is based on an assessment of potentially flaring active-region (AR) magnetic configurations, and it uses a sophisticated statistical analysis of a large number of AR magnetograms. For the prediction of SEP events, new statistical methods have been developed for the likelihood of the SEP occurrence and the expected SEP characteristics. The prediction window in the forecasting scheme is 24 hours with a refresh rate of 3 hours, while the respective prediction time for the nowcasting scheme depends on the availability of the near real-time data and ranges between 15 – 20 minutes for solar flares and 6 hours for CMEs. We present the modules of the FORSPEF system, their interconnection, and the operational setup. Finally, we demonstrate the validation of the modules of the FORSPEF tool using categorical scores constructed on archived data, and we also discuss independent case studies.

Combined Radio and Space-based Solar Observations: From Techniques to New Results
Guest Editors: Eduard Kontar and Alexander Nindos

✉ A. Anastasiadis
anastasi@noa.gr

[1] Institute for Astronomy, Astrophysics, Space Applications and Remote Sensing (IAASARS), National Observatory of Athens, I. Metaxa and Vas. Pavlou St., 15236, Penteli, Greece

[2] Research Center for Astronomy and Applied Mathematics (RCAAM), Academy of Athens, 4 Soranou Efesiou St., 11527, Athens, Greece

[3] Section of Astrogeophysics, Department of Physics, University of Ioannina, 45110 Ioannina, Greece

[4] European Space Research and Technology Centre (ESTEC), Space Environment and Effects Section Keperlaan 1, 2200AG Noordwijk, The Netherlands

Published online: 05 September 2017

Keywords Sun: coronal mass ejections (CMEs) · Sun: corona · Sun: radio radiation · Sun: solar energetic particle events · Sun: forecasting systems · Sun: integrated tools

1. Introduction

Solar eruptive events such as solar flares (SFs) and coronal mass ejections (CMEs) have a major space weather impact and affect the interplanetary (IP) and near-Earth environment through their high-energy processes and particles that are accelerated to near-relativistic energies, posing a threat to spacecraft, satellites, systems, and humans in space (*e.g.* Srour and McGarrity, 1988; Holmes-Siedle and Adams, 1993; Hapgood and Thomson, 2010). Solar flares are violent and intense variations in brightness taking place in active regions (ARs) that emit electromagnetic radiation (gamma- and X-rays) and accelerate energetic particles (protons and electrons) into space, while CMEs are bulk ejections of ultra-hot magnetized plasma that disrupt the solar wind, drive shock waves, and when they strike the Earth's magnetosphere, cause major, but transient, disturbances to the geomagnetic field. Both phenomena (solar flares and/or CMEs) accelerate particles to near-relativistic energies, resulting in enhanced levels of energetic particle fluxes that are termed solar energetic particle (SEP) events.

The nature of the solar flare prediction problem has resulted in research efforts applying a diverse array of techniques. Moreover, the categorization of flare prediction methods is not a trivial task (see Georgoulis, 2012). Flare prediction techniques can be viewed as comprising i) multiscale, ii) morphological, iii) statistical and historical, and iv) machine-learning and combinatorial methods. In particular, the multiscale behavior and the turbulence in photospheric AR magnetic fields indicate that flaring ARs display distinguishable complexity. Hence, this holds flare-predictive potential (Abramenko *et al.*, 2002, 2003; McAteer, Gallagher, and Ireland, 2005; Georgoulis, 2005; Uritsky *et al.*, 2007, 2013; Dimitropoulou *et al.*, 2009, among others). On the other hand, morphological flare-prediction methods rely on topological characteristics of eruptive solar ARs, such as the photospheric magnetic polarity inversion lines (PILs), intense magnetic-flux emergence, or photospheric properties in general (*e.g.* Falconer, Moore, and Gary, 2007; Schrijver, 2007; Georgoulis and Rust, 2007; Leka and Barnes, 2007; Mason and Hoeksema, 2010). Additionally, another morphological parameter is the effective connected magnetic field strength ($B_{\rm eff}$), originally proposed by Georgoulis and Rust (2007). $B_{\rm eff}$ is deduced using a magnetic connectivity map in the AR under study. Statistical methods are based on archived data, under the assumption that flare occurrence globally in the Sun is a time-dependent Poisson process (Moon *et al.*, 2001). Finally, the utilization of AR properties using machine-learning algorithms presents an enhanced ability of prediction that is driven by either a single or a combination of such properties. As an example in this direction, we name the automated solar activity prediction (ASAP) tool, operating at the University of Bradford (Qahwaji and Colak, 2007). In spite of the progress that has been achieved with respect to automated solar flare forecasting, the NOAA/Space Weather Prediction Center (SWPC) maintains a human-oriented, expert-based flare-prediction system.

Solar energetic particle events are observed as flux increases above a background level at different energies, ranging from ≈ 10 keV to ≈ 10 GeV/nuclei, which can last from a few hours to several days. SEPs consist of electrons, protons, alpha particles, and heavier ions up to Fe, and their propagation time to Earth spans from hours to a few days (Cane and Lario, 2006). They are produced either in the solar atmosphere by particle acceleration processes in association with powerful M- and X-class flares (Anastasiadis, 2002) and even

C-class flares (Krucker, White, and Lin, 2007; James, Subramanian, and Kontar, 2017) or in interplanetary (IP) shock waves created by the interaction of CMEs with the solar wind. The former are thought to produce short-lived ($\leq$ one day) impulsive events, while the latter produce much longer (gradual) events. Accelerated particles then propagate through the IP medium, spiraling along the IP magnetic field (IMF) lines. Since SEPs are the source of the most severe disturbances that can affect spacecraft, several techniques have been developed to predict the main characteristic parameters of an SEP event, such as onset time, peak flux, fluence, and duration (Smart and Shea, 1989; Balch, 1999, 2008; Laurenza *et al.*, 2009; Núñez, 2011, among others). However, owing to their sporadic nature ($\approx$ 100 *per* solar cycle), forecasting SEP events is not a trivial task, and the prediction schemes usually rely on a statistical data-driven approach with the corresponding relations built upon known features of solar eruptive events.

The activity that led to forecasting solar particle events and flares (FORSPEF) was supported through the European Space Agency (ESA), and its main focus was the implementation of forecasting tools for SEPs, solar flares, and CMEs. The current capabilities of the FORSPEF tool incorporate a novel integrated solution that provides forecasting of solar eruptive events, such as solar flares with a projection to CMEs (occurrence and velocity) and the probability of the occurrence of an SEP event. In addition, the tool provides short-term forecasting (nowcasting) of SEP events and their corresponding characteristics (peak flux, fluence, rise time, and duration), using as input actual SF and CME near real-time identifications. In Section 2 we present the modules and the operational set up; in Section 3 we provide the validation based on categorical scores, and finally, in Section 4 we present a discussion and the concluding remarks of this effort.

2. The FORSPEF Tool

The FORSPEF tool consists of three modules that aim to forecast i) the likelihood of upcoming solar flare eruptions, ii) the occurrence of SEPs by making a prediction of the time before onset, and iii) the SEP characteristics for an upcoming event, respectively. Additionally, it incorporates two operational modes, the forecasting and the nowcasting mode. The former is understood as the pre-event mode, since no actual solar event (*i.e.* solar flare or CME) has yet taken place. The only available information is the identification of an AR on the Sun and its calculated $B_{\rm eff}$ metric (see Section 2.1). The latter corresponds to the post-event mode, in which a solar event has actually taken place and its characteristics (for solar flares the longitude and the magnitude, and for CMEs the width and the velocity) are already available. FORSPEF offers a 24-hour forecast of SEP events, up to 70° E/W covering practically the entire course of the AR toward the limb (up to $\approx$ 85°), under the assumption that the AR does not change significantly over this course.

The FORSPEF tool is available online at http://tromos.space.noa.gr/forspef/ and provides continuous forecasts and nowcasts of SFs and SEP events. All outputs can be freely accessed and used by the scientific community.

2.1. Forecasting Solar Flares

The FORSPEF tool incorporates a solar flare forecasting module that delivers conditional flare probabilities complemented by information on CME probabilities and expected CME speeds. Flare probabilities rely on the "effective connected magnetic field strength" ($B_{\rm eff}$)

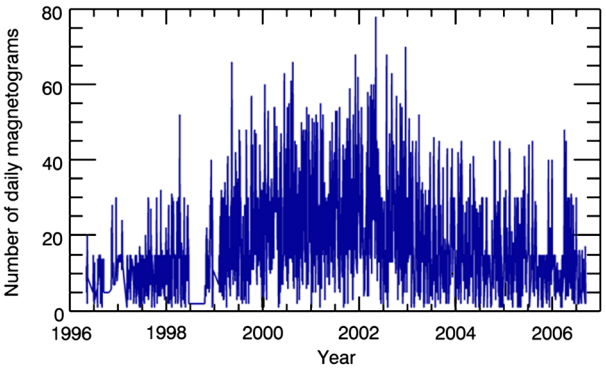

Figure 1 Daily SOHO/MDI magnetogram numbers of the solar flare module magnetogram sample. Practically the entire Solar Cycle 23 is included, with daily numbers of available magnetograms increasing notably during the maximum of the cycle.

prediction metric and stem from the previously collected statistics on the *Solar and Heliospheric Observatory* (SOHO)/*Michelson Doppler Imager* (MDI) B_{eff}-calculations. CME probabilities and projected speeds rely on the peer-reviewed published flare-to-CME association rates (Yashiro *et al.*, 2005) and on the statistical correlation between B_{eff}-values and recorded near-Sun CME velocities (Georgoulis, 2008), respectively. The statistics of flare prediction have been inferred from our collected SOHO/MDI database that spanned over the entire Solar Cycle 23. This SOHO/MDI database covers 2736 data-filled calendar days with 55691 magnetograms and 1416 different ARs (see Figure 1).

2.1.1. Data Provision and Eligible AR Identification

We download the latest SDO/*Helioseismic and Magnetic Imager* (HMI) full-disk magnetograms from the Joint Science Operation Center (JSOC) based at Stanford University, USA, the HMI Principal Investigator (PI) institution. Downloading was achieved via standard JSOC SolarSoft routines. Our active region identification algorithm (ARIA) was then used to automatically identify and crop eligible ARs. By "eligible" we mean ARs with a maximum tolerated magnetic flux imbalance[1] of 60% and a flux-weighted centroid location that is within 70° E/W on the solar disk. While this longitudinal zone serves to avoid the extreme near-limb areas where calculations with magnetic field are untenable, a maximum tolerated flux imbalance aims to select regions that show some significant bipolarity. Some sunspot regions are comprised of (unipolar) isolated sunspots connecting at relatively large distances, hence without major magnetic polarity inversion lines: we dismissed these regions because we do not expect significant eruptive activity to stem from them. We view the 60% flux-imbalance threshold as liberal enough to allow even strongly imbalanced ARs, at the same time dismissing mainly unipolar ones. A slightly different threshold will not incur a significant impact on the number of ARIA-identified regions. To proceed to the identification, ARIA i) smooths the full-disk line-of-sight (LOS) magnetogram using a window of $\approx$1 supergranular diameter (40″ or $\approx$ 30 Mm on the solar surface), ii) identifies flux accumulations in the original magnetogram that coincide with intensity-enhancements in the smoothed image, discarding accumulations with a magnetic flux imbalance higher than the above-prescribed maximum, iii) defines an intensity-weighted centroid for pinpointing each eligible intensity enhancement, iv) outlines each intensity enhancement and crops the eligible AR region, and v) assigns a National Oceanic and Atmospheric Administration (NOAA)

[1]Magnetic flux imbalance is defined as the ratio $\frac{\sum_i B_{zi}}{\sum_i |B_{zi}|}$. The summation refers to the entire AR area as identified by the ARIA.

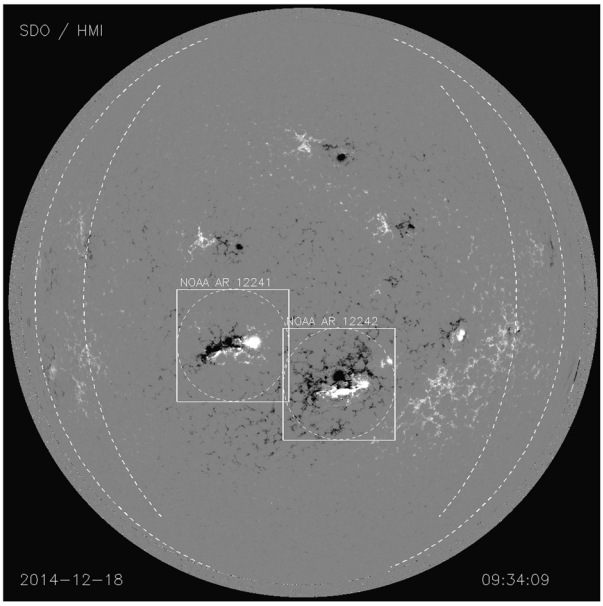

Figure 2 Sample pictorial ARIA output. Two solar ARs have been identified, labeled, and cropped. The two *thick dashed curves* in the E and W solar hemispheres indicate the 50° and 70° E and W solar meridians, respectively.

AR number to each identified AR by matching its centroid location with NOAA's, which is available online from the Space Weather Prediction Center (SWPC). To avoid extreme projection effects present in the observed LOS field component, ARIA considers only ARs with centroids within the above-mentioned meridional zone of ±70°. Figure 2 provides a typical output of ARIA with two major solar ARs identified, namely NOAA ARs 12241 and 12242.

2.1.2. Derivation of the $B_{\rm eff}$ Flare Prediction Metric

First, we pre-processed each HMI AR magnetogram to bring it as close as possible to what the MDI magnetograph would observe had it been in operation. In this respect, a rebinning to MDI resolution, instrumental features, and geometry were taken into account and a calibration in terms of absolute field strength was performed.

The "MDI-like" deprojected heliographic normal magnetic field component for each AR cutout was then used to calculate the $B_{\rm eff}$ value for the cutout. To achieve this, we implemented a magnetic flux-partitioning scheme that identifies the locations, outlines, and flux-weighted centroids of all non-overlapping positive- and negative-polarity flux accumulations. This is essentially a discretization of a continuous flux distribution into a discrete collection of N_+ and N_-, positive- and negative-polarity partitions, respectively, with known flux contents and topological properties, such as outlines and the location of the centroid. This is needed in order to derive the $[N_+, N_-]$ magnetic connectivity matrix Φ_{mn} that includes fluxes committed to connections between a positive-polarity partition m and a negative-polarity partition n with a connection length L_{mn} defined as the distance between the flux-weighted centroids of the two considered partitions. As the three-dimensional coronal magnetic field above the photospheric magnetogram is obviously unknown, the magnetic connectivity matrix Φ_{mn} is inferred *via* an iterative simulated-annealing method that defines connections between opposite-polarity flux partitions while globally minimizing the corresponding connection lengths L_{mn}. We note here that this is only one of many possible methods available to infer the magnetic connectivity matrix. It is our method of choice, however,

as the action of minimizing connection lengths emphasizes tightly seated opposite-polarity flux partitions, and it favors known photospheric flare-prolific patterns such as strong polarity inversion lines (PILs). In this scheme, ARs with intense PILs will exhibit higher $B_{\rm eff}$ values, and hence attain higher flare probabilities.

After we derived the connectivity matrix Φ_{mn}, the effective connected magnetic field strength $B_{\rm eff}$ for the studied AR at the given time is given by $B_{\rm eff} = \sum_{i=1}^{N_+} \sum_{j=1}^{N_-} \frac{\Phi_{ij}}{L_{ij}^2}$. As a result, $B_{\rm eff}$ collapses the two connectivity matrices, Φ_{mn} and L_{mn}, into a single scalar quantity, representative of a given AR at a given time.

Even though ARIA identifies ARs up to 70° E/W in central meridian distance, calculation of a $B_{\rm eff}$ value in the heliographic reference system is already problematic beyond 50° E/W because of very significant projection effects that give rise to a substantially deformed heliographic plane. In addition, the typical angular-position cosine-correction of the LOS field to obtain the local normal field is also known to have issues beyond 50°. Therefore, to infer a $B_{\rm eff}$ value for an AR within the meridional zone from 50° to 70° E/W, we used a proxy of $B_{\rm eff}$ that was obtained by the unsigned (total) magnetic flux of an AR. This flux is given by

$$\Phi_{\rm tot} = \iint_S \mid B_z \mid {\rm d}S, \tag{1}$$

with S corresponding to the FOV area. Using the SOHO/MDI database, we have found that $\Phi_{\rm tot}$ and $B_{\rm eff}$ are connected *via* the scaling,

$$B_{\rm eff} \approx 10^{-21.96} \Phi_{\rm tot}^{1.08}. \tag{2}$$

This proxy, of course, has much higher uncertainties because of the scatter of the $\Phi_{\rm tot}$ *versus* $B_{\rm eff}$ diagram, but is considered a reasonable compromise instead of lacking a $B_{\rm eff}$-value for ARs in the meridional zone 50 – 70° E/W altogether. For an average of ≈ 14° *per* day for each AR transit, this would correspond to ≈ 3 days of the AR presence in the earthward solar hemisphere. Detailed descriptions of ARIA can be found in LaBonte, Georgoulis, and Rust (2007) and Georgoulis, Raouafi, and Henney (2008).

2.1.3. Cumulative Flare Probabilities, CME Likelihoods, and Speeds

The calculated $B_{\rm eff}$ value for each AR was used to derive the respective cumulative flare probabilities for a certain GOES flare class and above. Our collected SOHO/MDI database corresponds to a sample of 55,691 AR magnetograms that belong to 1,416 ARs spanning the entire Solar Cycle 23, within 30° central meridian distance on the solar disk (Figure 1). These are associated with 4,574 flares in total, comprising 66 X-, 623 M-, and 3,885 C-class flares. Cumulative flare probabilities for each $B_{\rm eff}$ value are given by a sigmoidal fitting curve:

$$P_{\rm class}(B_{\rm eff_{(norm)}}) = A_2 + \frac{A_1 - A_2}{1 + \exp(\frac{\log B_{\rm eff(norm)} - X_0}{W})}. \tag{3}$$

In Equation 3, A_1, A_2, and X_0 are known fitting coefficients and W is the weight of the sigmoidal function. Here $B_{\rm eff_{(norm)}}$ is the normalized (with respect to the maximum $B_{\rm eff}$ value of the sample) $B_{\rm eff}$ threshold. The values of the coefficients A_1, A_2, X_0, and W vary with the targeted flare class (Figure 3, left-hand panel). With the conditional flare probabilities derived, the likelihood for a CME to accompany the predicted flare, or equivalently, the likelihood of this flare to be eruptive, was inferred from published flare-to-CME association

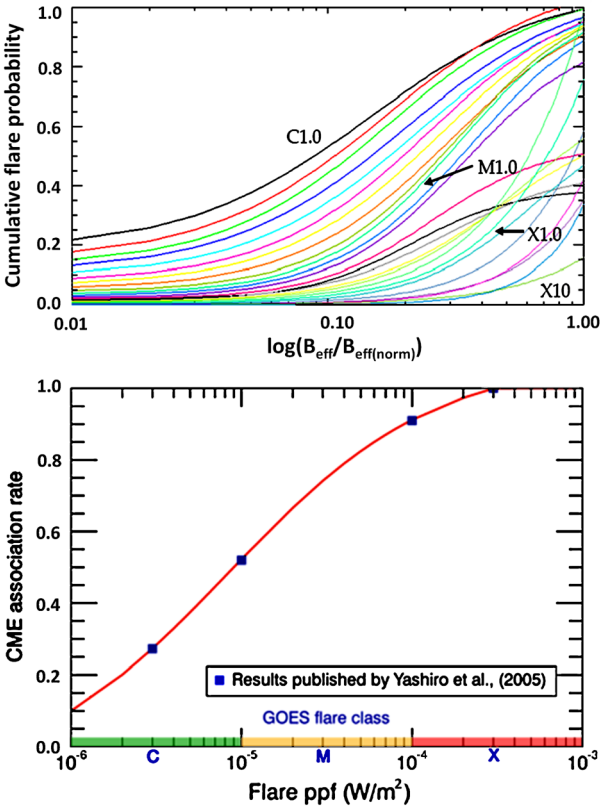

Figure 3 Fitting curves for all B_{eff} values and solar flare classes that are precalculated within the solar flare forecasting module (*left panel*) and the sigmoidal fit of the solar flare magnitude to the CME rate values, published by Yashiro and coworkers, see text for details (*right panel*).

rates (see Yashiro *et al.*, 2005). These rates can be fitted by another sigmoidal curve, and as a result, a cumulative flare probability p can be derived, which also has a CME associated rate p'. This will yield a likelihood for a CME or an eruptive flare equal to pp' (Figure 3, right-hand panel). Another independent piece of information we extracted is the projected near-Sun speed of the corresponding CME. This is based on the analysis of Georgoulis (2008) and again involved the B_{eff} value of the AR. It has indeed been found that near-Sun CME speeds V_{CME} are higher for higher B_{eff} values of the source ARs *via* the following fitting formula (see the bottom panel of Figure 2 of Georgoulis, 2008):

$$V_{\text{CME}} = 87.3\ B_{\text{eff}}^{0.38}\ [\text{km/s}]. \tag{4}$$

2.1.4. Output of the Solar Flare Forecasting and CME Likelihood Scheme

For each ARIA-identified solar AR, the output of the FORSPEF flare forecasting module is a structure containing the AR NOAA number, its heliographic and device-coordinate location, the corresponding B_{eff} value, the 24-hour cumulative flare probabilities for each of the 28 GOES flare classes (from C1.0 to X10.0) and their peak photon fluxes (PPFs), the respective eruptive-flare or CME likelihoods, and the projected CME velocity. The solar flare forecasting produces histogram curves of the cumulative flare probabilities and CME likelihoods *versus* the flare PPF. The cumulative forecast probabilities for flares (solid red

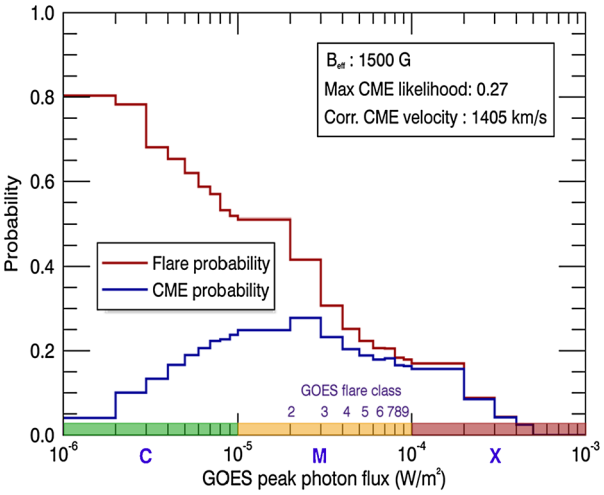

Figure 4 Pictorial output of the FORSPEF solar flare forecasting and likelihood of CME prediction scheme: shown are the 24-hour cumulative forecast probabilities for flares (*solid red histogram*) and CME likelihoods (*solid blue histogram*) for a sample AR. The legend provides further information on the calculated value of the B_{eff}, the maximum CME likelihood, and the corresponding CME velocity. Figure taken from Papaioannou *et al.* (2015).

histogram) and CME likelihood (solid blue histogram) for a sample AR are shown in Figure 4. For this case the maximum CME likelihood is $\approx 27\%$, with the projected near-Sun CME velocity estimated at ≈ 1405 km/s.

2.2. Forecasting Solar Energetic Particle Events

2.2.1. The FORSPEF Database of SEP Events, Solar Flares, and CMEs

The foundation of the FORSPEF SEP event prediction (either in the forecasting or in the nowcasting mode) is a new comprehensive database of SEP events, solar flares, CMEs, and radio fluxes (Papaioannou *et al.*, 2016), spanning from 1984 to 2013 (see Figure 5). The starting point of the database was the soft X-ray (SXRs) measurements from GOES and the CME information from the SOHO/*Large Angle and Spectrometric Coronagraph Experiment* (LASCO). We have applied spatial and temporal criteria to link SXRs and CMEs. Furthermore, we independently scanned GOES proton data of ≈ 10 MeV and identified 314 SEP events. The anticipated solar release time (SRT) was identified for each and every SEP event of the database, using the velocity dispersion analysis (VDA) (Vainio *et al.*, 2013). In order to pinpoint the solar sources(s) of the SEP event in question, in addition to the VDA, assessments with other published SEP lists as well as quantitative and qualitative checks were made. Our analysis is constructed on recently recalibrated GOES proton data (with IMP-8) that cover an energy range of 6 – 243 MeV (Sandberg *et al.*, 2014). More details on the database itself, together with an extended statistical analysis, are presented in Papaioannou *et al.* (2016).

2.2.2. The Kernel of SEP Prediction

In the forecasting (pre-event) scheme, the FORSPEF tool provides the probability of SEP occurrence based on the information delivered by the solar flare forecasting (*i.e.* the cumulative solar flare probabilities). The work flow is the following: for a given location of an AR, the solar flare forecasting module provides a cumulative probability function (CDF) over all 28 GOES solar flare classes (see Figure 4). For this given AR location, the nearest (in longitude) 4000 historical solar flare events stored in the FORSPEF SEP database are identified.

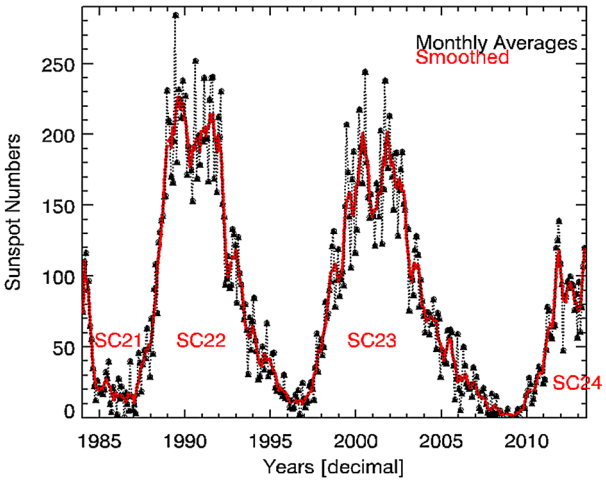

Figure 5 Time span of the FORSPEF database of SEP events, solar flares, CMEs, and radio flux. It covers ≈ 30 years and spans almost three solar cycles. The solar cycles are presented *via* the monthly averaged sunspot number (*black trace*) and their smoothed curve (*red line*).

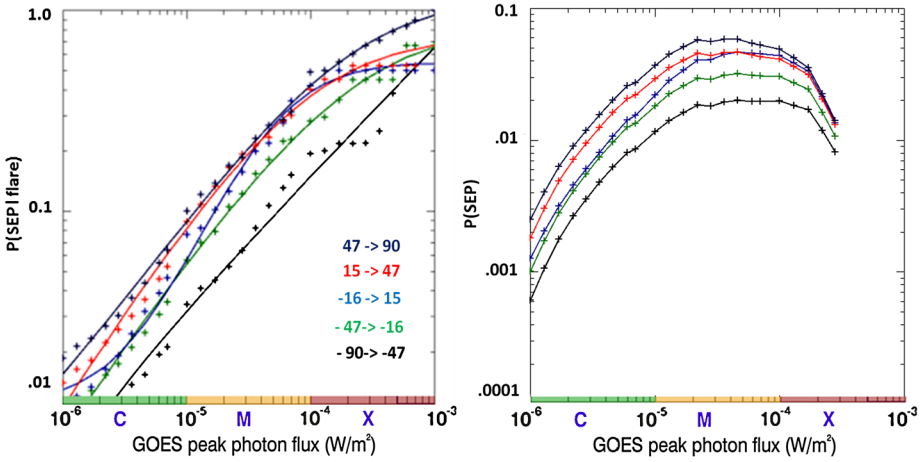

Figure 6 Example of the distribution functions (DFs) obtained from the FORSPEF database, *per* longitudinal bin over 28 GOES SXRs bins (*left panel*). The folding of the output of the FORSPEF database with the output of the solar flare forecasting provides the probability of SEP occurrence (*right panel*) *per* longitudinal bin. This latter plot is the output of FORSPEF's SEP forecasting. The FORSPEF tool provides the maximum probability as defined by the respective folded curve *per* longitudinal bin.

Figure 6 illustrates the procedure of establishing the local SEP model. Five longitudinal bins cover the whole visible disk of the Sun. For each longitudinal bin, the historical 4000 flares are used in order to derive a probability of SEP occurrence *per* solar flare magnitude defined as $P(\mathrm{SEP}_{\mathrm{flare}})_i = (N_{\mathrm{SEP}})_i/(N_{\mathrm{all}})_i$ with $i = [1, 28]$ covering all 28 GOES bins of the solar flare forecasting. These $P(\mathrm{SEP}_{\mathrm{flare}})_i$ values are used to implement a local SEP statistical model *via* distribution functions (DFs). The values are further fitted with a sigmoidal fit. The derived probabilities and their corresponding sigmoidal fits are presented in Figure 6. These probabilities depend on the FORSPEF database alone and not on the output of the solar flare forecasting module.

As a next and final step, the FORSPEF tool provides a weighted forecast for the expected occurrence of an SEP event *per* AR, calculated as the product of the local SEP module and the cumulative solar flare probabilities as identified in Figure 4 (solid red curve). The output of the SEP forecasting (pre-event) scheme is the maximum probability for each of the considered ARs. This is presented in the right panel of Figure 6, which shows the folded probability of SEP occurrence from the FORSPEF database with the output of SF forecasting (Figure 4). A detailed example of the FORSPEF SEP forecasting workflow is presented in Papaioannou *et al.* (2015). A SEP forecast (pre-event) window is 24 hours, while forecasts are renewed every three hours or more frequently.

2.3. Nowcasting of Solar Energetic Particle Events

Nowcasting is the short-term forecasting that is triggered by a solar eruptive event, *i.e.* solar flare or CME, with known characteristics. Hence, nowcasting is also characterized as a post-event mode. FORSPEF has developed two operational nowcasting modules – one that is based on near real-time solar flare information (longitude, magnitude) and another module that makes use of near-real time CME data (width, velocity). Furthermore, FORSPEF implements another module that is non-operational in real-time mode. This is based on the short-term forecasting concept introduced by Laurenza *et al.* (2009) and was recently further refined and validated by Alberti *et al.* (2017). In this latter work this nowcasting scheme is called ESPERTA.

2.3.1. Nowcasting Based on Solar Flares

For a given solar flare with known characteristics (longitude and magnitude), the data reserved in the FORSPEF database are used in order to extract the DFs in the nowcasting (post-event) scheme. For each spotted SF, the nearest (in longitude) 4000 historical solar flare events are identified in the FORSPEF SEP database, as before. These are used to implement the local statistical SEP model and to derive the SEP occurrence probability from the FORSPEF SEP database, similar to the forecasting mode.

Furthermore, the FORSPEF database also stores pre-calculated SEP characteristics (peak-flux, fluence) for all of its 314 SEP events in four integral energy channels ($E > 10$; > 30; > 60; > 100 MeV) (Papaioannou *et al.*, 2016). These values are used to statistically calculate the SEP-projected characteristics (*e.g.* maximum of the peak flux, time of maximum of the peak flux, duration, and fluence) of the expected forthcoming SEP event. Therefore, probable median values of the SEP characteristics (currently median values are used, although the mean, 25th and 75th percentiles are also calculated and stored in the FORSPEF system) are offered to the end-users of the FORSPEF tool.

The detection of SEP events, in terms of the occurrence probability, is performed based on the actual near real-time solar flare data (*i.e.* maximum solar flare magnitude and position) that is routinely downloaded in near-real time mode from Solar Demon (http://solardemon.oma.be/flares.php), a service operated by the Royal Observatory of Belgium (ROB) (Kraaikamp and Verbeeck, 2015). A typical nowcast (post-event) warning window is on the order of $\approx 15-20$ minutes, while nowcasts are renewed with the identification of any new solar flare event. The inputs of the FORSPEF nowcasting work-scheme are in practice the outputs of the Solar Demon service, in particular the maximum flare flux and its position (longitude) on the visible part of the solar disk. FORSPEF makes use of all $\geq$ C1.0 flares spotted by this service.

2.3.2. *Nowcasting Based on CMEs*

In order to examine the SEP occurrence probability based on CME characteristics, we divided SEPs and their associated CMEs from the FORSPEF database into nine subgroups according to the CME speed (three groups: slow, moderate, and fast CMEs) and CME angular width (three groups: full-halo, partial-halo, and non-halo CMEs). Our results show that the probabilities increase with CME speed and angular width. The probability of all nine subgroups is 8.08% (154/1905). The highest probability is 72.7% for the subgroup with fast and full-halo CMEs. The lowest probability is 0.7% for the subgroup of CMEs with slow and non-halo CMEs. Further details on this module are presented in the recent work of Papaioannou *et al.* (2017).

Within the operation point of view, this nowcasting scheme uses the near real-time outputs provided online through the computer-aided CME tracking software (CACtus) (Robbrecht and Berghmans, 2004; Robbrecht, Berghmans, and Van der Linden, 2009), operated by ROB. The refresh rate of the outputs provided by CACtus is approximately six hours, based on the CME cadence by SoHO/LASCO, but nonetheless, CACtus is the only near real-time CME solution that provides reliable and continuous outputs that can be used as seeders from SEP nowcasting efforts, such as the FORSPEF tool.

2.3.3. *Nowcasting Based on the ESPERTA Model*

In this scheme we used the method proposed by Laurenza *et al.* (2009) (ESPERTA model) (Alberti *et al.*, 2017) to indicate whether a solar eruption will produce an SEP event surpassing 10 pfu at an integral energy of $E > 10$ MeV, based on the solar flare location, the SXR integrated flux (SXR fluence), and the radio-integrated flux at ≈ 1 MHz (*i.e.* radio fluence). Our effort mainly focused on calculating the integrated radio and SXR flux for all solar flares (see Figure 7) of the FORSPEF database within Solar Cycle 23 with a magnitude of > M1.0. For much of Solar Cycles 23 and 24, WIND/WAVES data were considered in this part of the work, with 0.944 MHz being the closest frequency to 1 MHz at which measurements were routinely made. We provide refined calculations of the radio and SXR fluxes based on the SFs and SEP events in the FORSPEF database. We additionally applied a regression probabilistic model (see Equation 5), similar to Laurenza *et al.* (2009), and we obtained the relevant refined equations that could lead to the SEP occurrence prognosis:

$$P\big(\log(x_1), \log(x_2)\big) = \frac{\mathrm{e}^n}{1+\mathrm{e}^n}, \tag{5}$$

with $n = b_0 + b_1 x_1 + b_2 x_2 + b_3 x_1 x_2$, and x_1 the integrated SXR flux, and x_2 the integrated radio flux.

However, we note that the ESPERTA model has not yet been integrated into the operational FORSPEF tool, since the radio data from WIND/WAVES are not available in near real-time. Nevertheless, in case such data are made available in the future, this can be achieved.

3. Validation of the FORSPEF Tool

The validation of the FORSPEF tool was based on the calculation of categorical scores (*i.e.* probability of detection – POD, false-alarm rate – FAR, Heidke skill score – HSS, overall

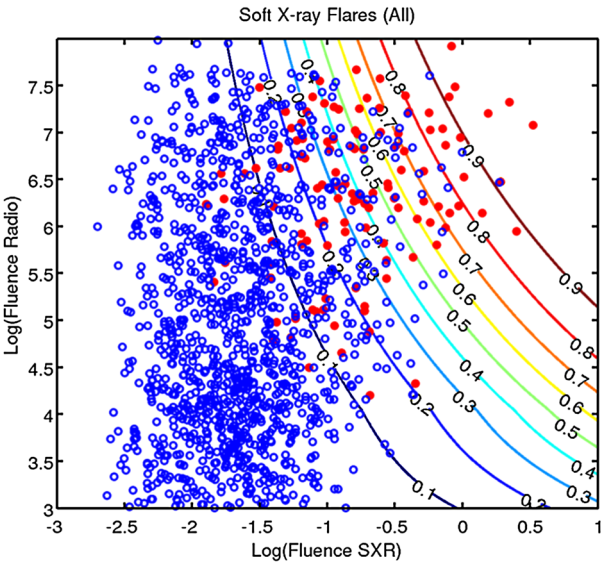

Figure 7 Probability contours for SEP forecasting based on the ESPERTA concept, using the FORSPEF database of SEP events, solar flares, and CMEs. Solar flares associated with SEPs are illustrated as *filled red circles*, while solar flares not associated with SEPs are presented as *open blue circles*. The sample covers > 1422 solar flares with magnitude $\geq$ M1.0. The overplotted contours represent different probabilities as these are obtained from Equation 5.

accuracy – OA, critical success index – CSI, percent correct – PC, true skill statistics – TSS). For consistency, we present the categorical score definitions in Appendix A. For a detailed discussion, we refer to the WWRP/WGNE Joint Working Group on Forecast Verification Research, available at http://www.cawcr.gov.au/projects/verification/.

3.1. Solar Flare Forecasting

To validate the $B_{\rm eff}$-based solar flare prediction scheme, we used contingency tables that applied to dichotomous/categorical forecasting. To populate the contingency table and infer skill scores, we took a threshold, $p_{\rm thres}$ for the $B_{\rm eff}$-based flare probabilities starting from 0.05 and ending at 0.95 with increments of 0.05 for all GOES flare classes (C1 – X10). In all cases, achieving $p \geq p_{\rm thres}$ ($p < p_{\rm thres}$) implies a YES (NO) flare forecast. From this analysis, we deduced that the significant values of the achieved skill scores and in particular, values of HSS and TSS, peak at ≈ 0.4 and ≈ 0.5, respectively. Moreover, peak TSS values are typically slightly or significantly higher than peak HSS values. As expected, for higher performance, misses and false positives should both be restricted to low values, ideally lower than those of hits. The great majority of entries in the contingency table are classified as true negatives, which can be understood from the fact that only a slim minority of ARs flare with PPFs $\geq$C1.0.

In Figure 8 we show the six skill-score values plotted as functions of the probability threshold for three reference GOES flare classes, namely C1, M1, and X1. We note that HSS and TSS both peak at $p_{\rm thres} \approx 0.4$ for C-class flares and above, while for much lower $p_{\rm thres}$ values for flares $\geq$ M1.0 and $\geq$ X1.0 they peak at 0.15 – 0.20 and 0.05 – 0.10, respectively. These $p_{\rm thres}$ values are critical skill-scores peaks that can be used to specify which predictive probabilities can be characterized as most significant, if achieved. These are the probabilities for which forecasting comes as close as possible to a dichotomous YES/NO prediction.

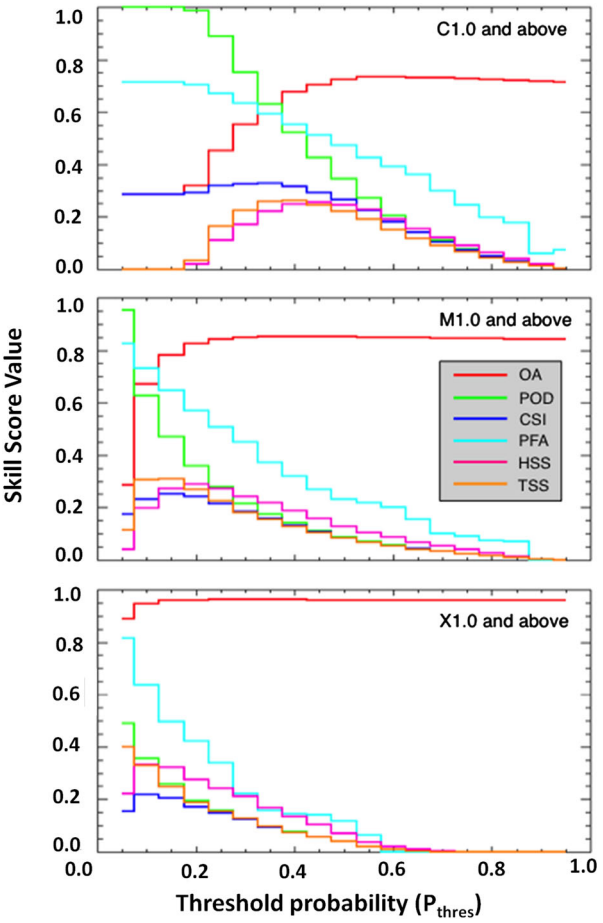

Figure 8 Skill-score values obtained for three reference GOES flare classes (C1 *top*; M1 *middle*; X1 *bottom*) as a function of the probability threshold p_{thres} adopted to construct the respective contingency tables. A forecast window of 24 hours holds for all cases.

3.2. Solar Energetic Particle Event Nowcasting Modules

3.2.1. Probabilities of Detection

For the post-event nowcasting mode, categorical measures were calculated. For the control and test sample of events, the time interval from the beginning of Solar Cycle 23, *i.e.* 1997 to the end of the FORSPEF database (*i.e.* 2013), was chosen. This is because we were in need of a time span that could be used as the basis of the validation, but also for the intercomparison between the different submodules of the nowcasting mode. There were 10,026 solar flares, 3,680 different CMEs, 174 SEP events, and 150 Type III bursts[2] within this time span in the FORSPEF database of SEP events, solar flares, and CMEs. Of these, we selected $\approx 90\%$ (9026 solar flares) of the solar flares as the control sample, and the rest (10%) were treated as the test sample, with the selection of the test and control samples being

[2]Type III bursts signify the propagation of beams of nonthermal electrons in the solar atmosphere and the solar system. As a result, they provide information on electron escape, acceleration, and transport, as well as on the conditions of the background ambient plasma they travel through.

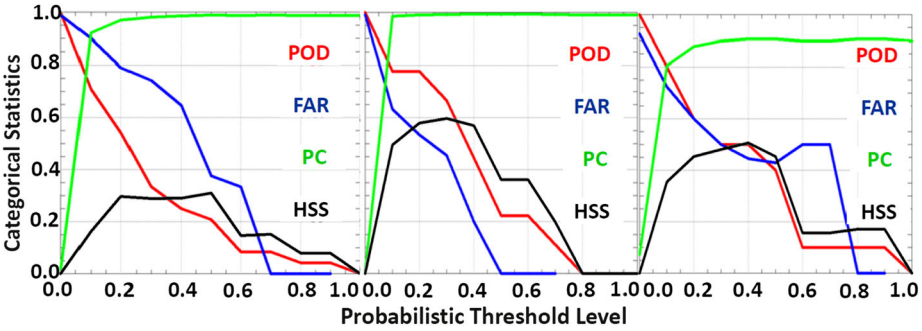

Figure 9 Categorical performance statistics for FORSPEF's nowcasting mode, based on solar flare input (*left panel*), CME data (*middle panel*) and radio and SXR integrated fluence data (*right panel*), as a function of the probability threshold.

Table 1 Mean values of the HSS, POD, FAR, and pt for the ten independent test samples.

FORSPEF nowcasting based on	HSS	POD	FAR	pt
Solar flare data	0.37 ± 0.011	0.40	0.57	0.25
CME data	0.67 ± 0.007	0.71	0.41	0.25
Radio and SXR fluence data	0.47 ± 0.04	0.55	0.42	0.28

completely random. This procedure was repeated ten times, and we obtained ten different – completely independent – control and test samples.

We considered next the performance categorical quality measures for POD, FAR, HSS, and PC, which are defined as functions of the probability threshold (pt). All categorical scores were derived for all test samples with the categorical measures calculated using the solar flare, the CME, and the integrated radio and SXRs flux information as input to the corresponding submodules of the nowcasting mode.

Indicative examples are presented in Figure 9. Specifically, the panel on the left refers to the submodule based on solar flare data, the middle panel to the submodule based on CME data, and the panel on the right to the submodule based on radio and SXRs fluence data (the ESPERTA concept). An examination of all three plots shows that FAR decreases when pt increases, but at the expense of POD, which is also decreasing with increasing threshold (Balch, 2008).

We also note that the optimal skill score (using HSS) is achieved for all three submodules at the range of probabilities (pt) from 20% to 30% (specific mean values of pt *per* submodule are presented in Table 1). This result is consistent with the literature (*i.e.* Balch, 2008). However, there is a clear possibility to enhance the accuracy of the predictions since even at the optimal pt value, false alarms and missed events are both far from insignificant. Furthermore, it seems that the higher mean POD was achieved for the CME submodule (0.71) with a mean FAR of 0.41. Nonetheless, the scores also demonstrate the actual operational capabilities of the FORSPEF tool *per* submodule, since they rely on solar flare and CME information – which is the only precursor information available continuously in near real-time mode.

Next we investigated specific case studies. We examined the October–November 2003 period – known as the "Halloween Events", including five consecutive SEP events (Jiggens *et al.*, 2014), and the events on 20 January 2005 (Bütikofer *et al.*, 2008) and the 07 March

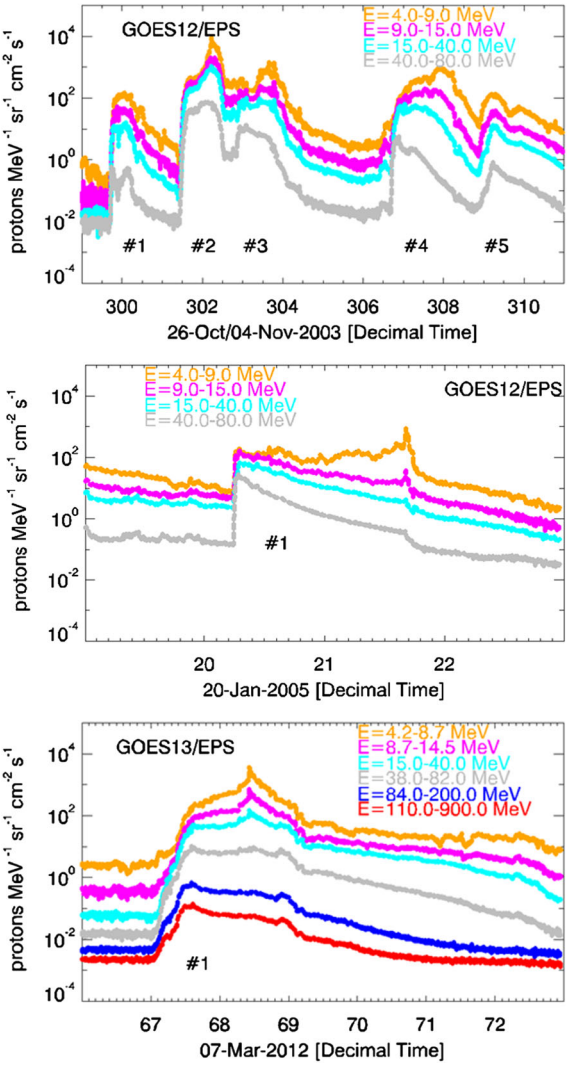

Figure 10 Case studies used in this part of the study. From top to bottom we present the time profiles of the five consecutive "Halloween" SEP events that were recorded onboard GOES/EPS at an energy range of 4.0 – 80.0 MeV (*top panel*); the time profile of the SEP event of 20 January 2005 – again at the same energy range (*middle panel*); and the time profile of the SEP event of 07 March 2012 identified onboard GOES/EPS at a wider energy range from 4.0 – 900 MeV (*bottom panel*).

2012 (Patsourakos *et al.*, 2016). These events had characteristic signatures in the low- and high-energy channels and have been extensively analyzed by the scientific community. In Figure 10 we present plots of these events as recorded onboard GOES/EPS, ranging from 4 – 80 MeV in all cases, with the exception of the event of 07 March 2012, which was recorded up to the highest available EPS energies.

Using the associated parent solar events as input parameters for these SEP events (Papaioannou *et al.*, 2016), we derived the probability of SEP detection *per* case (event) and *per* module. Figure 11 presents the obtained outputs. The blue histogram denotes the outputs of the CME module, the orange histogram displays the outputs of the solar flare module, and the red histogram presents the outputs of the ESPERTA module. The pt thresholds above which an alert/notification would have been issued are presented with a continuous (CME, solar flare modules) and a dotted (ESPERTA module) line, as identified above (see Table 1).

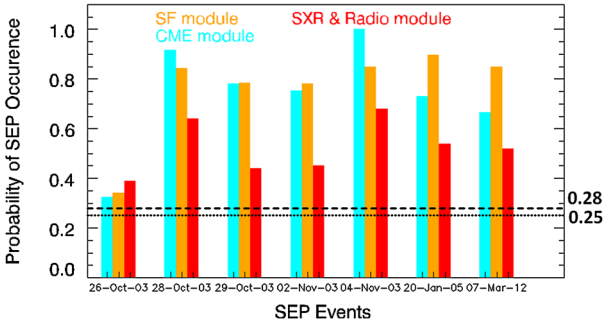

Figure 11 Comparison of the predicted probabilities of SEP detection *per* module, under the nowcasting mode for all seven case studies presented in Figure 10. The *blue histogram* represents the outputs of FORSPEF's nowcasting mode based on CME data, the *orange histogram* represents the outputs of the mode based on solar flare data, and the *red histogram* represents the outputs of the mode based on the ESPERTA concept. The *horizontal lines* represent the thresholds above which the modules would issue a notification for a forthcoming SEP event – see text for details.

As a result, it seems that all three FORSPEF nowcasting modules would spot all of these events.

3.2.2. Characteristics of SEP Events

As a next step, the predicted flux at $E > 30$; $E > 60$ and $E > 100$ MeV for all SEP events in the FORSPEF database with complete flare information (*i.e.* longitude and flux) was calculated. In what follows, the predicted peak flux *versus* the observed peak flux *per* energy is presented (Figure 12).

The predicted peak flux at any energy can be calculated statistically and represented *via* the median (50%), the lower (25th percentile), and the upper (75th percentile) limit. In what follows, the top row of Figure 12 represents the predicted peak flux at the lower limit as a function of the observed peak flux at all energies, *i.e.* $E > 30$, $E > 60$, and $E > 100$ MeV (magenta), the middle row represents the same plots, but for the median value (red), and the bottom row represents the same plots for the upper limit (blue). The predicted peak flux at $E > 30$ MeV as a function of the observed peak flux at the same energy shows a weak correlation since the correlation coefficient (cc) is calculated to be 0.256 (lower limit), 0.332 (median), and 0.321 (upper limit). Although there is significant scatter from the perfect dichotomous prediction line, most of the time the predictions are within one order of magnitude of the observations, but not always (Figure 12, first column). The same results for the predictions as a function of the observed flux at $E > 60$ and $E > 100$ MeV follow in Figure 12, in the middle and right columns, respectively. The *ccs* are slightly better ($cc = 0.394$ (lower limit), 0.410 (median), 0.406 (upper limit), and $cc = 0.370$ (lower limit), 0.374 (median), and 0.402 (upper limit)), but the important feature here is that small events are dominant and with much less scatter about the perfect prediction line.

In addition, the predicted flux at $E > 30$, $E > 60$, and $E > 100$ MeV for all SEP events in the FORSPEF database with complete CME information (*i.e.* velocity and width) was calculated. In what follows, the predicted peak SEP flux as a function of the corresponding observed value *per* energy is presented in Figure 13.

The predicted peak flux at $E > 30$ MeV as a function of the observed peak flux at the same energy shows a relatively strong correlation since the correlation coefficient is cal-

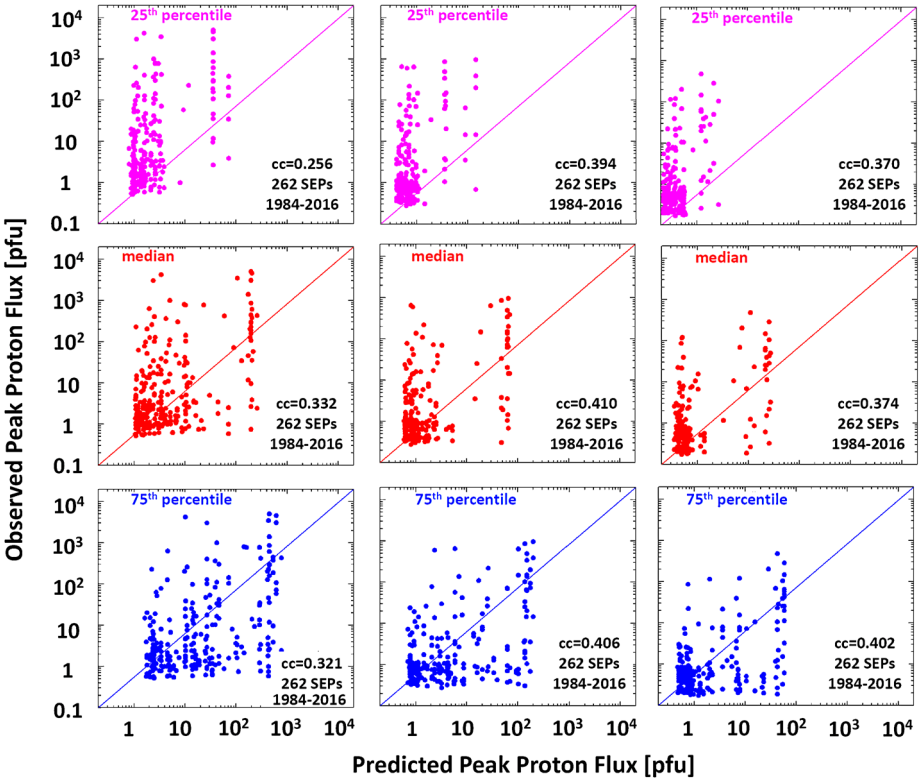

Figure 12 Comparison of predicted with observed peak flux for 262 SEP events from 1984 – 2013. The *middle row* provides the comparison for the predicted median value, while the *top row* represents the lower limit (25th percentile) and the *bottom row* the upper limit (75th percentile).

culated to be 0.55. Although there is significant scatter of the points about the perfect dichotomous prediction line, it seems that there is a tendency for underforecasting, since the difference between the predicted and the observed values is within a factor of ≈ 3, but not always (Figure 13). The same results for the predicted as a function of the observed flux at > 60 and > 100 MeV follow in Figure 13, in the middle and right panels, respectively. The *ccs* are slightly degrading ($cc = 0.49$ ($E > 60$ MeV) and 0.43 ($E > 100$ MeV)).

4. Discussion and Conclusions

The FORSPEF tool is a new operational open-access forecasting system that provides reliable forecasting and nowcasting of SEP events, as well as forecasting of SFs based on precursor information. Given the two operational modes of the tool, FORSPEF provides expected probabilities of SEP occurrence using either the outputs of the solar flare forecasting or the near real-time solar event identifications.

The basic implementations of the FORSPEF tool presented in this study are summarized as follows:

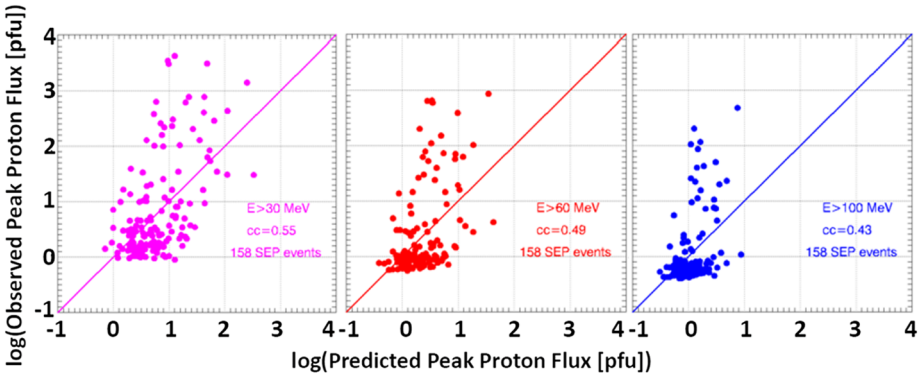

Figure 13 Comparison of predicted with observed peak flux for 158 SEP events from 1996 – 2013, based on CME input data.

- To predict solar flares, FORSPEF incorporates a module that makes use of the effective connected magnetic field strength prediction metric ($B_{\rm eff}$). The corresponding statistics are based on an extended database of magnetograms that covers Solar Cycle 23.
- The prognosis of SEP events is based on a new database of SEP events and their parent solar events (*i.e.* SFs and CMEs). This comprehensive database covers an extended time span from 1984 – 2013, and brings together solar and particle observations coupling the events at the Sun to those detected at 1 AU.
- From an inferred flare probability for a single AR, we obtain a respective CME probability.
- On a region-*per*-region basis, we coupled this probability with CME velocity information and assessed the likelihood of CME shock formation thus.
- Furthermore, coupling the SF probability with a local DF obtained *via* the FORSPEF database of SEPs, solar flares, and CMEs, we assessed the likelihood of an SEP event in geospace 24hr in advance.
- Three modules were developed for short-term forecasting of SEP events and their corresponding characteristics, based on solar flare, CME, and radio flux data.

All components of the FORSPEF tool were validated based on archived data. As a first step, we validated the forecasting/nowcasting modules using an extensive statistical study on a significant large archived sample of solar flare, CME, radio flux, and SEP events. We constructed categorical scores for the predictions issued by the different modules, with the analysis performed on randomly selected training and trial samples. Furthermore, we included scatter plots of observed *versus* predicted SEP properties (characteristics) to quantify the capabilities of the tool.

Additionally, as a second step, we investigated detailed case studies of significant SEP events that have previously been reported in the literature. Blind tests with archived parent solar data of these events were applied to the various modules of the FORSPEF tool in order to derive the probabilities of SEP detection *per* module and *per* event.

The real-time results of FORSPEF are assessed in both textural and pictorial form through the web portal http://tromos.space.noa.gr/forspef/.

Acknowledgements This work was supported through the ESA Contract No. 4000109641/13/NL/AK "Improvement of Solar Particle Events and Flare Prediction". AA acknowledges the support through "SPECS: Solar Particle Events and foreCasting Studies" research grant of the National Observatory of Athens. The

authors would like to thank Karl-Ludwig Klein and Angels Aran for constructive discussions. This article uses data from the CACTus CME catalog and the Solar Demon tool, generated and maintained by the Solar Influences Data Analysis Center (SIDC) at the Royal Observatory of Belgium (ROB). The provision of the SDO/HMI data by the Stanford Solar Group is also gratefully acknowledged.

Disclosure of Potential Conflict of Interest The authors declare that they have no conflicts of interest.

Appendix A: Categorical Scores

In general, in order to derive categorical scores, we need to enable the construction of contingency tables and to calculate the various skill scores stemming from them. We imposed thresholds on predictive probabilities above/below which a YES/NO prediction was adopted, and we inferred the skill scores as a function of these thresholds. However, the application of categorical measures to probabilistic forecasts requires the definition of a probabilistic threshold, pt. If the forecast/nowcast probability is $\geq$ pt, a warning is issued, while if the forecast/nowcast probability is $<$ pt, no warning is issued. Based on this, it is possible to construct a contingency table (see Table 2) and calculate event-based norms.

For our purposes of validation, we used the following scores:

- The overall accuracy (OA) with a perfect score of 1 achieved in the case that there are no misses and no false positives: $\mathrm{OA} = a + d/N$.
- The probability of detection (POD), which ignores false positives and true negatives and achieves a perfect score of 1 in the case that there are no misses: $\mathrm{POD} = a/a + c$.
- The critical success index (CSI), which ignores true negatives and achieves a perfect score of 1 in the case that there are no false positives and no misses: $\mathrm{CSI} = a/a + b + c$.
- The probability of a false alarm (PFA) or false-alarm rate (FAR), which ignores misses and true negatives and achieves a perfect score of 0 in the case that there are no false positives: $\mathrm{FAR} = \mathrm{PFA} = b/a + b$.
- The Heidke skill score (HSS), which was used to quantify the ability of achieving correct predictions with respect to chance. A value of 0 or lower implies that correct predictions could be completely due to chance, while a perfect score of 1 is achieved in the opposite case: $\mathrm{HSS} = 2(ad - bc)/(a + c)(c + d) + (a + b)(b + d)$.
- The percent correct (PC), which provides the ratio of correct predictions as a percentage of the total number of forecasts: $\mathrm{PC} = a + c/N$.
- The true skill statistic (TSS) obtains values in the range $[-1, 1]$ with a perfect score of 1 attained in the case that there are no false positives and no misses (same as CSI),

Table 2 Classical 2×2 contingency table for dichotomous forecasting on a total of N predictions. Table elements correspond to (a) hits, corresponding to events that were predicted and observed, (b) false positives or false alarms, corresponding to events that were predicted but not observed, (c) misses, corresponding to events that were not predicted but observed, and (d) true negatives, corresponding to events that were neither predicted nor observed.

Event forecast	Event observed		
	YES	NO	Marginal total
YES	a (hits)	b (false positives)	$a + b$
NO	c (misses)	d (true negatives)	$c + d$
Marginal total	$a + c$	$b + d$	$a + b + c + d = N$

and a totally unskilled value of -1 attained in the case that there are no hits and no true negatives. A value of 0 demonstrates equal "sensitivity" to hits, compared to false positives, and misses, compares to true negatives: $\mathrm{TSS} = a/(a+b) - c/(c+d)$.

For probabilistic forecasts, we can treat the probability threshold, pt, as an independent variable ranging within [0.0, 1.0] and calculate the categorical scores (POD, FAR, HSS, and PC) *per* pt value. It is expected to identify a decrease of FAR while pt increases. At the same time, however, a decrease in POD is also marked. The optimal score is traced using HSS for a value of pt.

References

Abramenko, V.I., Yurchyshyn, V.B., Wang, H., Spirock, T.J., Goode, P.R.: 2002, *Astrophys. J.* **577**, 487. DOI.

Abramenko, V.I., Yurchyshyn, V.B., Wang, H., Spirock, T.J., Goode, P.R.: 2003, *Astrophys. J.* **597**, 1135. DOI.

Alberti, T., Laurenza, M., Cliver, E.W., Storini, M., Consolini, G., Lepreti, F.: 2017, *Astrophys. J.* **838**(1), 59. http://stacks.iop.org/0004-637X/838/i=1/a=59.

Anastasiadis, A.: 2002, *J. Atmos. Solar-Terr. Phys.* **64**, 481. DOI.

Balch, C.C.: 1999, *Radiat. Meas.* **30**(3), 231.

Balch, C.C.: 2008, *Space Weather* **6**(1), S01001. DOI.

Bütikofer, R., Flückiger, E., Desorgher, L., Moser, M.: 2008, *Sci. Total Environ.* **391**(2), 177.

Cane, H.V., Lario, D.: 2006, *Space Sci. Rev.* **123**, 45. DOI.

Dimitropoulou, M., Georgoulis, M., Isliker, H., Vlahos, L., Anastasiadis, A., Strintzi, D., Moussas, X.: 2009, *Astron. Astrophys.* **505**, 1245. DOI.

Falconer, D., Moore, R., Gary, A.: 2007, In: *American Astronomical Society Meeting Abstracts #210*, *Bulletin of the American Astronomical Society* **39**, 135.

Georgoulis, M.K.: 2005, *Solar Phys.* **228**, 5. DOI.

Georgoulis, M.K.: 2008, *Geophys. Res. Lett.* **35**, L06S02. DOI.

Georgoulis, M.K.: 2012, *Astrophys. Space Sci. Proc.* **30**, 93. DOI.

Georgoulis, M.K., Rust, D.M.: 2007, *Astrophys. J. Lett.* **661**, 109. DOI.

Georgoulis, M., Raouafi, N.-E., Henney, C.: 2008, *ASP Conf. Ser.* **383**, 107.

Hapgood, M., Thomson, A.: 2010, *Space weather: Its impact on earth and implications for business*, Lloyd's 360 Risk Insight.

Holmes-Siedle, A., Adams, L.: 1993, Handbook of radiation effects.

James, T., Subramanian, P., Kontar, E.P.: 2017, *Mon. Not. Roy. Astron. Soc.* **471**(1), 89. DOI.

Jiggens, P., Chavy-Macdonald, M.-A., Santin, G., Menicucci, A., Evans, H., Hilgers, A.: 2014, *J. Space Weather Space Clim.* **4**, A20.

Kraaikamp, E., Verbeeck, C.: 2015, *J. Space Weather Space Clim.* **5**, A18.

Krucker, S., White, S.M., Lin, R.P.: 2007, *Astrophys. J. Lett.* **669**(1), L49. http://stacks.iop.org/1538-4357/669/i=1/a=L49.

LaBonte, B., Georgoulis, M., Rust, D.: 2007, *Astrophys. J.* **671**(1), 955.

Laurenza, M., Cliver, E.W., Hewitt, J., Storini, M., Ling, A.G., Balch, C.C., Kaiser, M.L.: 2009, *Space Weather* **7**, S04008. DOI.

Leka, K.D., Barnes, G.: 2007, *Astrophys. J.* **656**, 1173. DOI.

Mason, J.P., Hoeksema, J.T.: 2010, *Astrophys. J.* **723**, 634. DOI.

McAteer, R.T.J., Gallagher, P.T., Ireland, J.: 2005, *Astrophys. J.* **631**, 628. DOI.

Moon, Y.-J., Choe, G.S., Yun, H.S., Park, Y.D.: 2001, *J. Geophys. Res.* **106**, 29951. DOI.

Núñez, M.: 2011, *Space Weather* **9**(7).

Papaioannou, A., Anastasiadis, A., Sandberg, I., Georgoulis, M.K., Tsiropoula, G., Tziotziou, K., Jiggens, P., Hilgers, A.: 2015, *J. Phys. Conf. Ser.* **632**(1), 012075. http://stacks.iop.org/1742-6596/632/i=1/a=012075.

Papaioannou, A., Sandberg, I., Anastasiadis, A., Kouloumvakos, A., Georgoulis, M.K., Tziotziou, K., Tsiropoula, G., Jiggens, P., Hilgers, A.: 2016, *J. Space Weather Space Clim.* **6**(27), A42. DOI.

Papaioannou, A., Anastasiadis, A., Sandberg, I., Jiggens, P.: 2017, *J. Space Weather Space Clim.*

Patsourakos, S., Georgoulis, M., Vourlidas, A., Nindos, A., Sarris, T., Anagnostopoulos, G., Anastasiadis, A., Chintzoglou, G., Daglis, I., Gontikakis, C., *et al.*: 2016, *Astrophys. J.* **817**(1), 14.

Qahwaji, R., Colak, T.: 2007, *Solar Phys.* **241**, 195. DOI.

Robbrecht, E., Berghmans, D.: 2004, *Astron. Astrophys.* **425**(3), 1097.
Robbrecht, E., Berghmans, D., Van der Linden, R.: 2009, *Astrophys. J.* **691**(2), 1222.
Sandberg, I., Jiggens, P., Heynderickx, D., Daglis, I.A.: 2014, *Geophys. Res. Lett.* **41**, 4435. DOI.
Schrijver, C.J.: 2007, *Astrophys. J. Lett.* **655**, 117. DOI.
Smart, D.F., Shea, M.A.: 1989, *J. Spacecr. Rockets* **26**, 403. DOI.
Srour, J.R., McGarrity, J.M.: 1988, *Proc. IEEE* **76**(11), 1443.
Uritsky, V.M., Paczuski, M., Davila, J.M., Jones, S.I.: 2007, *Phys. Rev. Lett.* **99**(2), 025001. DOI.
Uritsky, V.M., Davila, J.M., Ofman, L., Coyner, A.J.: 2013, *Astrophys. J.* **769**, 62. DOI.
Vainio, R., Valtonen, E., Heber, B., Malandraki, O.E., Papaioannou, A., Klein, K.-L., Afanasiev, A., Agueda, N., Aurass, H., Battarbee, M., Braune, S., Dröge, W., Ganse, U., Hamadache, C., Heynderickx, D., Huttunen-Heikinmaa, K., Kiener, J., Kilian, P., Kopp, A., Kouloumvakos, A., Maisala, S., Mishev, A., Miteva, R., Nindos, A., Oittinen, T., Raukunen, O., Riihonen, E., Rodríguez-Gasén, R., Saloniemi, O., Sanahuja, B., Scherer, R., Spanier, F., Tatischeff, V., Tziotziou, K., Usoskin, I.G., Vilmer, N.: 2013, *J. Space Weather Space Clim.* **3**(27), A12. DOI.
Yashiro, S., Gopalswamy, N., Akiyama, S., Michalek, G., Howard, R.A.: 2005, *J. Geophys. Res.* **110**, A12S05. DOI.